

# Robust edge-directed interpolation of magnetic resonance images

Zhenhua Mai<sup>1</sup>, Jeny Rajan<sup>1</sup>, Marleen Verhoye<sup>2</sup> and Jan Sijbers<sup>1</sup>

<sup>1</sup> IBBT-Visionlab, Physics Department, Universiteit Antwerpen, Belgium

<sup>2</sup> Bio-Imaging Lab, Biomedical Department, Universiteit Antwerpen, Antwerpen, Belgium

E-mail: [zhenhua.mai@ua.ac.be](mailto:zhenhua.mai@ua.ac.be)

Received 8 July 2011, in final form 26 September 2011

Published 28 October 2011

Online at [stacks.iop.org/PMB/56/7287](http://stacks.iop.org/PMB/56/7287)

## Abstract

Image interpolation is intrinsically a severely under-determined inverse problem. Traditional non-adaptive interpolation methods do not account for local image statistics around the edges of image structures. In practice, this results in artifacts such as jagged edges, blurring and/or edge halos. To overcome this shortcoming, edge-directed interpolation has been introduced in different forms. One variant, new edge-directed interpolation (NEDI), has successfully exploited the ‘geometric duality’ that links the low-resolution image to its corresponding high-resolution image. It has been demonstrated that for scalar images, NEDI is able to produce better results than non-adaptive traditional methods, both visually and quantitatively. In this work, we return to the root of NEDI as a least-squares estimation method of neighborhood patterns and propose a robust scheme to improve it. The improvement is twofold: firstly, a robust least-squares technique is used to improve NEDI’s performance to outliers and noise; secondly, the NEDI algorithm is extended with the recently proposed non-local mean estimation scheme. Moreover, the edge-directed concept is applied to the interpolation of multi-valued diffusion-weighted images. The framework is tested on phantom scalar images and real diffusion images, and is shown to achieve better results than the non-adaptive methods as well as NEDI, in terms of visual quality as well as quantitative measures.

(Some figures in this article are in colour only in the electronic version)

## 1. Introduction

Image interpolation (upsampling) aims to resolve the unknown, high-resolution (HR) pixels from the known, low-resolution (LR) pixels. Since the LR image is an approximation of the HR image, interpolation is an inverse problem. Additionally, as the number of unknown

HR pixels usually exceeds that of the known LR pixels, it is in general an ill-posed problem. Certain models concerning the relation between HR and LR pixels will have to be used in order to determine the HR pixels from the LR ones (Thévenaz *et al* 2000). The most widely used interpolation methods (Lehmann *et al* 1999), such as bi-linear interpolation (Meijering 2002) and bicubic interpolation (Keys 1981), readily employ global space-invariant models that fail to respect the local statistics around the edges in the image. Consequently, they produce artifacts such as jagged edges, blurring and/or edge halos (Thévenaz *et al* 2000). Moreover, valid structural information can be lost during the interpolation by bi(tri)-linear or even bi-cubic interpolation, as shown in Chao *et al* (2009).

In order to improve the interpolation quality, numerous methods based on more sophisticated models have been proposed (Lee and Paik 1993, Jensen and Anastassiou 1995, Allebach and Wong 1996, Morse and Schwartzwald 1998, Wang and Kreidieh 2007, Li and Orchard 2001b). Adaptive interpolation techniques (Lee and Paik 1993) exploit the relation of local image intensities, with ‘warped distance’, to adapt the linear interpolation coefficients to better capture local features around the edges. Edge-directed interpolation (EDI) techniques (Jensen and Anastassiou 1995, Allebach and Wong 1996, Morse and Schwartzwald 1998, Wang and Kreidieh 2007) employ models that extract edge information in order to guide the interpolation in different ways. The edge information is often extracted explicitly, for example, in Jensen and Anastassiou (1995), and a parameterized edge model is used to predict the HR edge information from the detected LR edge information. Alternatively, in Allebach and Wong (1996), an HR edge map is first generated by filtering the input LR data, and the HR image is generated with constraints from the HR edge map. This approach is similarly exploited in Morse and Schwartzwald (1998) by means of extracting isophotes, or iso-contours, from the LR image. Furthermore, in Wang and Kreidieh (2007), the edge orientations are extracted and grouped into a finite set to guide the final interpolation.

Unfortunately, the pitfall of edge-interpolated techniques aforementioned is that they have to explicitly extract the edge information and/or discretize the interpolation direction into a finite set. The successful extraction of edge information still presents a challenge to date, especially for certain low-contrast medical images. Also for multi-valued images such as diffusion-weighted images (DWI), the definition of ‘edge’ is far from straightforward, in contrast to the scalar case. Moreover, a finite set of interpolation directions can prove to be artificial and unstable.

In order to avoid the problems associated with explicitly estimating edges, Li *et al* proposed to exploit the ‘geometric duality’ between the covariance of a LR image and a HR image, with the help of linear prediction theory, and guide the interpolation with the implicitly retained edge information in covariance (Li and Orchard 2001b). Harnessing the mathematical elegance, their method (new edge-directed interpolation, NEDI) is able to produce results both visually pleasing and quantitatively competitive. However, because of the ordinary least-squares nature of NEDI, it is not robust for outliers. In the presence of heavy noise, this drawback will further severely hamper the performance of NEDI, as we will discuss more in detail in later sections. In this work, we utilize a robust least-squares technique to improve this drawback. Furthermore, since NEDI uses a least-squares fit of the pattern of the neighborhoods to achieve optimal interpolation, we make the connection between NEDI and the non-local mean (NLM) method (Buades *et al* 2005). As is shown, NLM can provide a measure of the similarity between neighborhood patterns. The NLM concept is incorporated into our algorithm such that it links directly to the improved least-squares framework of NEDI.

As an application, our proposed interpolation method is applied to DWI MR images. Diffusion MR image processing tasks involve interpolations in both pre- and post-processing stages. As mentioned previously, traditional interpolation methods are shown to be liable to

lose image structural information. Moreover, interpolation is further complicated by the low signal-to-noise ratio, which is characteristic for DWI (Basser and Pajevic 2000a), in which the magnitude MR images are plagued by the Rician noise (Gudbjartsson and Patz 1995) (as opposed to the typical Gaussian noise in the common digital images). Sophisticated techniques have already been developed to upsample the diffusion MR images in the slice direction (Mai *et al* 2010), while for in-plane upsampling the traditional bi(tri)-linear interpolation methods are still the most commonly used in practice. By contrast, our algorithm is shown to preserve the image structure for diffusion MR image interpolation.

This paper is organized as follows. Section 2 covers our methodology. Firstly, section 2.1 briefly introduces NEDI; secondly, section 2.2 details our reinterpretation of NEDI as a least-squares method, and then section 2.3 provides the details of our improvements based on the new understanding of NEDI. In section 3, experiments on phantom images, synthetic brain images and real MR brain images are described. Finally, in section 4, conclusions are drawn, and prospects for future work are given.

## 2. Methods

First, it should be noted that while the original NEDI algorithm is 2D based, there is no algorithmic barrier that hinders its extension to 3D images. However, in this work, we limit our attention to 2D images and treat the 3D volumes as a series of 2D slices. This is out of consideration that multi-slice MR images, especially DW images, typically have thick slices, as compared to the much smaller in-plane pixel dimension.

### 2.1. New edge-directed interpolation

We assume the LR image  $x_{i,j}$  of dimensions  $W \times H$ , defined on a domain  $\Omega$  with  $\Omega = \{(i, j) | 1 \leq i \leq W, 1 \leq j \leq H\}$ , to be a downsampled version of the HR image  $y_{2i-1,2j-1}$  of dimension  $(2W - 1) \times (2H - 1)$ , i.e.  $y_{2i-1,2j-1} = x_{i,j}$ , as shown in figure 1. The goal of interpolation is to compute pixel intensities  $y_{2i,2j}$ ,  $y_{2i-1,2j}$  and  $y_{2i,2j-1}$ . Let us consider for example the reconstruction of  $y_{2i,2j}$ . It is assumed that this value can be reconstructed from its immediate  $n \times n$  neighbors (without loss of generality,  $n$  is taken to be 2 in the following) by a weighted sum:

$$\hat{y}_{2i,2j} = \sum_{k=0}^1 \sum_{l=0}^1 \alpha_{2k+l} x_{i+k, j+l}, \quad (1)$$

where  $\alpha_{2k+l}$  is the weight of each neighbor pixel  $x_{i+k, j+l}$  in determining  $y_{2i,2j}$ . According to the classical Wiener filtering theory (Jayant and Noll 1984), the optimal linear interpolation coefficients are given by

$$\boldsymbol{\alpha} = \mathbf{R}^{-1} \mathbf{r}, \quad (2)$$

where  $\boldsymbol{\alpha}$  is the vector containing weights  $\alpha_i$ , and  $\mathbf{R}$  and  $\mathbf{r}$  are the local covariances (Li and Orchard 2001a) at HR, which are unknown. However, assuming the so-called ‘geometric duality’ (Li and Orchard 2001a), the correspondence between the HR covariance and the known LR covariance can be established, so that the HR covariance can be estimated from the LR one. Therefore, we have

$$\mathbf{R} = \frac{1}{N} \mathbf{C}^T \mathbf{C}, \quad \mathbf{r} = \frac{1}{N} \mathbf{C}^T \mathbf{x}, \quad (3)$$

where  $\mathbf{x} = [x_1, x_2, x_3, x_4]^T$  is the neighbor vector that contains the  $N$  (4 in this case) immediate neighbors of pixel  $y_{2i,2j}$ . Using the correspondence between the LR and HR images as shown

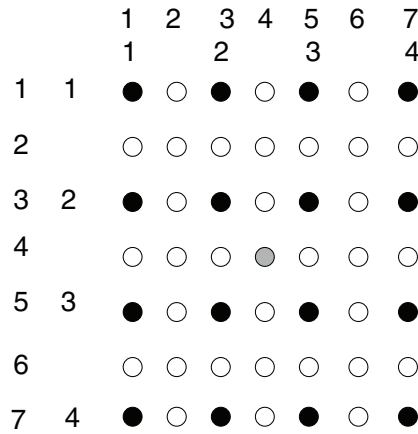


**Figure 1.** The overlay of the image domains of LR and HR image. Black pixels are the known  $y_{2i-1,2j-1}$  pixels (HR image, outer index), which coincide with the  $x_{i,j}$  pixels (LR image, inner index). Center gray pixel  $(y_{4,4})$  and other white pixels ( $y_{2i,2j}$ ,  $y_{2i-1,2j}$  and  $y_{2i,2j-1}$ ) are to be determined.

in figure 1,  $\mathbf{x}$  can be replaced with  $\mathbf{y} = [y_1, y_2, y_3, y_4]^T$ , where  $y_i$  is the corresponding known HR pixel of the LR pixel  $x_i$ .  $\mathbf{C}$  is the  $4 \times N$  matrix, the  $k$ th ( $k \leq N$ ) row of which contains the four neighbors of  $y_k$ . Then, the weights  $\alpha_i$  can be estimated from  $\mathbf{C}$  and  $\mathbf{y}$  as follows:

$$\boldsymbol{\alpha} = (\mathbf{C}^T \mathbf{C})^{-1} (\mathbf{C}^T \mathbf{y}). \quad (4)$$

For pixels  $y_{2i-1,2j}$  and  $y_{2i,2j-1}$ , the computations are similar, except for a rotation and scaling of the neighborhood (Li and Orchard 2001b). It is worth noting that according to the original NEDI paper, the computation outlined previously is only performed on pixels for which the standard deviation of the intensities of its neighbors is larger than a certain threshold. This, as a crude form of edge detection, helps to alleviate the computational load, while still avoiding estimating edges explicitly. We have retained this mechanism in the implementation of our algorithm.

## 2.2. NEDI reinterpreted as least-squares fitting

Here we continue the discussion by looking at the NEDI formula, equation (4), from another view point. Equation (4) was derived from the Wiener filtering theory (Jayant and Noll 1984). However, we can immediately see that equation (4) is actually the solution to a least-squares problem:

$$\hat{\boldsymbol{\alpha}} = \arg \min_{\boldsymbol{\alpha}} \|\mathbf{y} - \mathbf{C} \boldsymbol{\alpha}\|^2. \quad (5)$$

Now let us further decompose the above-vectorized formula:

$$\hat{\boldsymbol{\alpha}} = \arg \min_{\boldsymbol{\alpha}} \left\| \begin{bmatrix} r_1 \\ r_2 \\ r_3 \\ r_4 \end{bmatrix} \right\|^2 = \arg \min_{\boldsymbol{\alpha}} \left\| \begin{bmatrix} y_1 \\ y_2 \\ y_3 \\ y_4 \end{bmatrix} - \begin{bmatrix} y_{1,1} & \cdots & y_{1,4} \\ y_{2,1} & \cdots & y_{2,4} \\ y_{3,1} & \cdots & y_{3,4} \\ y_{4,1} & \cdots & y_{4,4} \end{bmatrix} \times \begin{bmatrix} \alpha_1 \\ \alpha_2 \\ \alpha_3 \\ \alpha_4 \end{bmatrix} \right\|^2, \quad (6)$$

where  $r_i$  is the residual for each fit:  $r_i = y_i - [y_{i,1}, \dots, y_{i,4}] \cdot \boldsymbol{\alpha}$ . Following the logic in equation (1), we can interpret the weights  $\boldsymbol{\alpha}$  as characteristics of the pattern of a pixel's

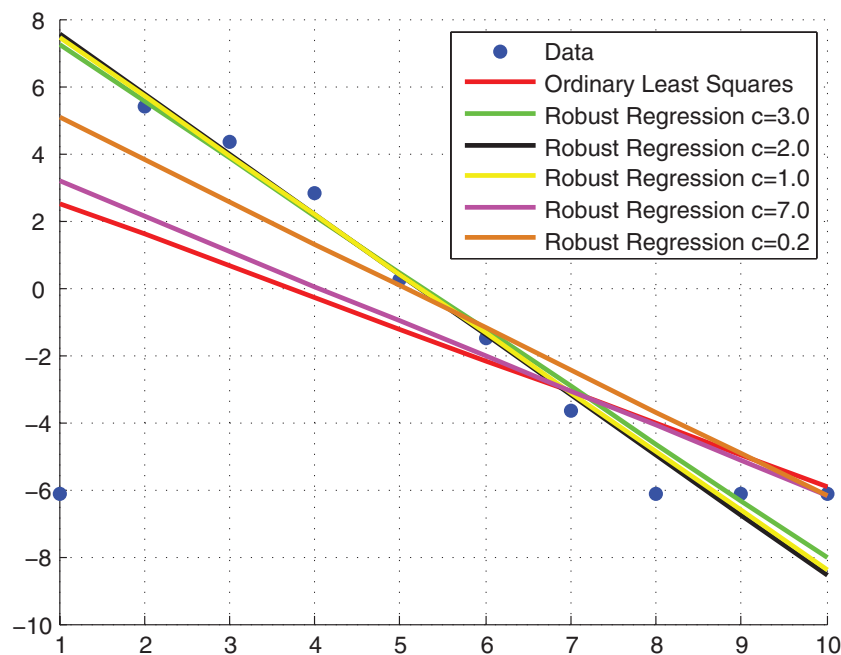


**Figure 2.** A comparison of 1D data fitting between OLS and the robust iterative reweighted least-squares (IRLS) technique (or robust regression). Blue points indicate the original discrete data points, which construct a slanted edge structure, with additive noise. The first one and the last two data points are outliers outside of the edge. The red line is the result from OLS fitting. For the IRLS fittings, the green line is the result for  $c = 3.0$ , black line for  $c = 2.0$ , yellow line for  $c = 1.0$ , magenta line for  $c = 7.0$  and brown line for  $c = 0.2$ .

surrounding neighbors. Therefore, the meaning of equation (4) becomes much clearer: what it achieves is a least-squares fit of the patterns of the neighborhoods (row elements in  $C$ ) in the search area spanned by  $y$ .

With NEDI interpreted as such, we now look at the algorithm (and its flaws) from another point of view. As is well documented, ordinary least-squares (OLS) estimation as used in the original NEDI is far from robust, and liable to the influence of outliers and/or noise (Zhang 1997). While the presence of noise is obviously detrimental to the image interpolation task, ‘outliers’ in the context of NEDI are those pixels that do not belong in the same edge, as do other edge pixels. For a 1D demonstration, see figure 2. As shown in figure 2, the presence of noise and ‘outliers’ in the computation might consequently undermine the ability of NEDI to discern the edge and guide the interpolation. We will detail the improvements we propose with respect to this shortcoming of NEDI in the following section.

### 2.3. Robust NEDI

In this section, we propose two improvements to the original NEDI algorithm. Firstly, the estimation is made robust with respect to outliers and/or noise. Secondly, NLM weighting is incorporated for performance improvement.

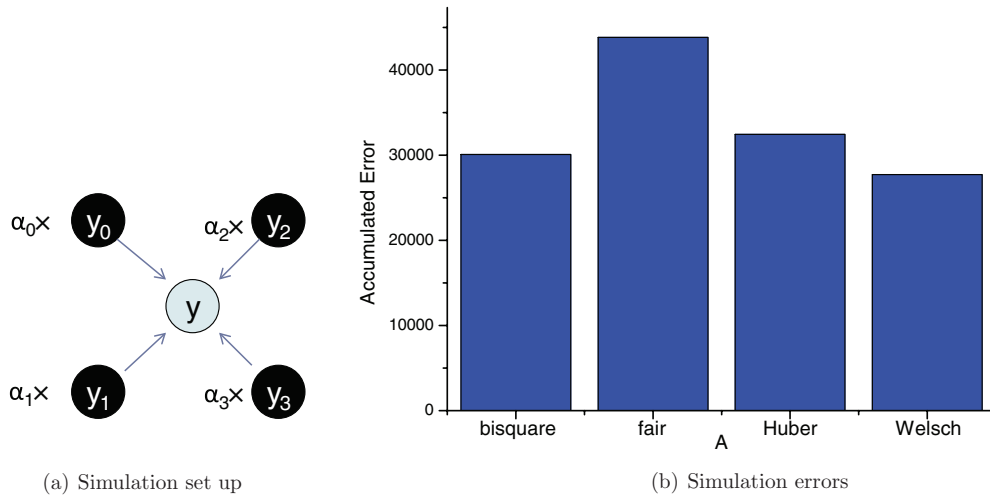


**Figure 3.** A simulation test for determining the optimal weighting function.

**2.3.1. Robust IRLS fitting.** In the literature, numerous methods to overcome the non-robustness of OLS estimation have been proposed (Zhang 1997). In our work, we start from the well-known IRLS fitting method (Holland and Welsch 1977). In IRLS, the sum of the squared residuals, weighted with a function of the residuals from the previous iteration, is iteratively minimized, i.e.

$$\alpha^{(k)} = \arg \min_{\alpha^{(k)}} \sum_i \omega^R(r_i^{(k-1)})(r_i^{(k)})^2, \quad (7)$$

where the superscript  $(k)$  indicates the iteration  $k$ . The function  $\omega^R(x)$  is a monotonically non-increasing function of  $x$ .

The most commonly used weighting functions include the ‘bisquare function’, ‘Huber function’, ‘fair function’ and ‘Welsch function’. For a complete description of each function, readers are referred to (Zhang 1997). Since the choice of the weighting function is application-dependent and crucial for the outcome, we conducted a simulation test to determine the optimal weighting function. The simulation was set up as in figure 3(a), in which a 4-neighborhood setup was used. The intensities of the four pixels,  $y_i$  ( $0 \leq i \leq 3$ ), were randomized between a preset range,  $Y_{im} \leq y_i \leq Y_{iM}$ . The intensity of the central pixel  $Y$  was then set as a weighted sum, with weights  $\alpha$  fixed and known. Each IRLS testing, with different weighting functions, was supplied with 15 datasets of neighbors and central pixels (which were corrupted with 10% Rician noise and 10% outliers), in order to perform a robust regression to estimate weights  $\alpha^R$ . The error in weights estimation can then be computed as  $\|\alpha - \alpha^R\|$ . This simulation was repeated 100 000 times, and the accumulated errors for each IRLS with different weighting function are shown in figure 3(b). From this test, we can conclude that the ‘Welsch function’ is preferable to other functions, and it is adopted in the final implementation of this work.

The power of IRLS can be effectively shown in a 1D demonstration in figure 2, where the weighting function is taken to be the ‘Welsch function’ (Zhang 1997),  $\omega^R(x) = e^{-x^2/c^2}$ , with  $c$  controlling the weighting function’s behavior with respect to outliers. According to (Zhang 1997), setting  $c = 2.98546$  can achieve an optimal asymptotic efficiency. In figure 2, where

the IRLS fitting results for different  $c$  are shown, it is found that  $c$  values clustering around the aforementioned optimum value would result in more or less the same fitting results, while values that deviate far from that (for example, when  $c = 0.2$  or  $7.0$ ) would result in similar results as in OLS. Therefore, we adopt the value as recommended in the literature.

**2.3.2. NLM weighting.** Since we have reinterpreted NEDI as a least-squares fit of the neighborhood patterns, it is desirable to maximize its ability for doing so, while keeping in mind the context for ‘robustness’. The newly emerged NLM algorithm (Buades *et al* 2005) proved promising for this purpose. The NLM algorithm was designed specifically for denoising purposes, whose success is largely due to its ability to differentiate between non-local neighborhood patterns (non-local ‘patches’). In other words, the NLM algorithm estimates the underlying, noiseless pixel values from its non-local neighboring pixels based on the similarity of their corresponding neighborhoods. Despite the algorithmic difference, this is the same principle as NEDI, especially after our reinterpretation. Furthermore, NLM does so with robustness and efficiency. We therefore apply NLM to our algorithm, by incorporating it into the reweighting part of the least-squares fit. The NLM-weighted iterative least-squares fit will take the following form:

$$\alpha^{(k)} = \arg \min_{\alpha^{(k)}} \sum_i \omega_i^N \cdot \omega^R(r_i^{(k-1)}) \cdot (r_i^{(k)})^2, \quad (8)$$

where  $\omega_i^N$  is the NLM weight function (Buades *et al* 2005) and is expressed as

$$\omega_i^N = e^{-\frac{\|N^i - N^{\text{current}}\|^2}{h^2}}, \quad (9)$$

where  $N^i$  stands for the vector that contains the intensities of the neighborhood of the  $i$ th pixel,  $N^{\text{current}}$  that of the neighborhood of the current pixel, and  $h$  controls the smoothness of the NLM weight function.

According to Buades *et al* (2005), in a typical denoising application of the NLM,  $h \approx 10 \cdot \sigma$ , where  $\sigma$  is the standard deviation of the noise in the image. For our specific application of NLM for interpolation purpose, we conducted experiments to ascertain the optimal  $h$ . As shown in figure 4, we tested with different  $h$  values (as a factor of noise standard deviation  $\sigma$ ) on synthetic phantom images (see section 3) with different  $\sigma$  being 10% (black), 20% (red) and 30% (blue) of the mean intensity of the synthetic image. The optimal  $h$  values, in terms of peak signal-to-noise ratio (PSNR,  $Y$  axis), are found to coincide on  $h = 1 \cdot \sigma$ , as indicated by the indigo line in figure 4. This indicates a uniform scale factor of 1 when it comes to decide the value of  $h$  as a function of  $\sigma$ , regardless of the noise levels (our experiments suggest that the factor of 1 also applies to cases with different upsampling factors, different images, etc). Note that the scale factor of 1 is also in accordance with further developments of the NLM algorithm in the denoising application, e.g. Manjón *et al* (2008). Figures 5(a)–(c) show sample images from our NLM weighting influence test: figure 5(a) without NLM weighting, figure 5(b) robust IRLS with optimal NLM weighting, and figure 5(c) with excessive NLM weighting (with high  $h$ ). The artifacts in figure 5(a) mainly come from the singular results during the IRLS computation, which is caused by inappropriately assigning edge-pixels and non-edge pixels into the estimation. It can be seen that with NLM weighting, the interpolation result is more smooth, and less artifact-prone, while oversmoothing with a high  $h$  tends to lose structural details. Since part of the neighborhood pixel values are originally unknown, the computation in equation (8) has to be iterative. For the pseudo-code of the NLM weighted IRLS fitting, see figure 6.

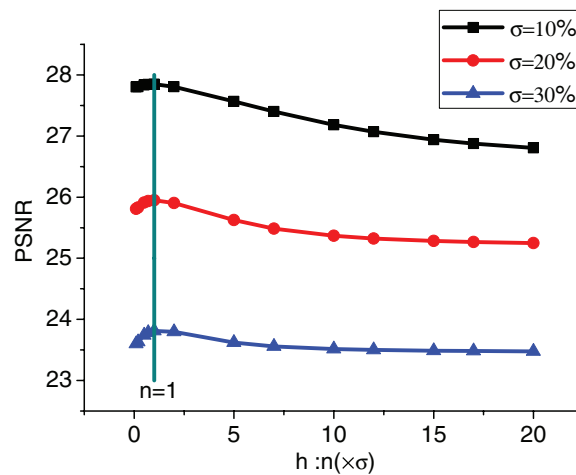


**Figure 4.** A demonstration of the impact of different  $h$  values on interpolation. The  $h$  values used are factors of the standard deviation of the noise  $\sigma$ . Noise levels used are 10% (black), 20% (red) and 30% (blue) of the mean intensity of the synthetic image.

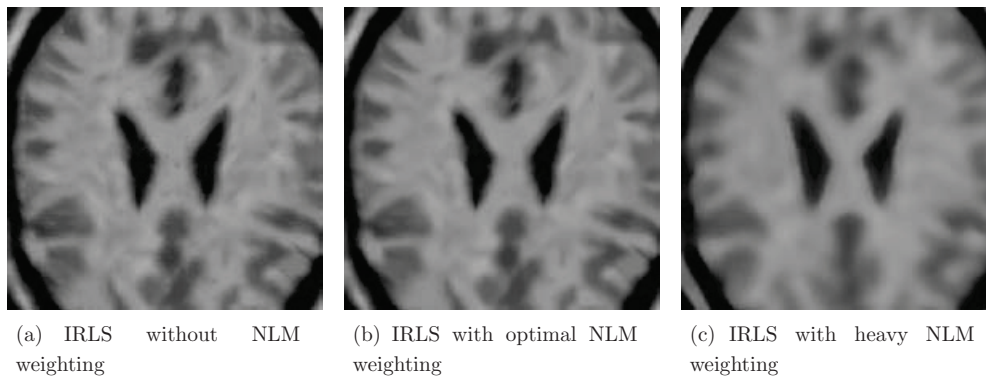


**Figure 5.** A demonstration of the impact of different NLM weightings on the interpolation. (a)–(c) Sample images from our NLM weighting influence test: (a) without NLM weighting, (b) the robust IRLS with optimal NLM weighting and (c) with excessive NLM weighting (high  $h$ ).

With the two proposed improvements, our algorithm is able to distinguish robustly between neighborhoods of different intensity patterns. As a simple example, we show in figure 7 an edge pattern, where four sample neighborhoods are considered. It is easy to see that the drastic difference between  $N_2$  and other neighborhood regions ensures that  $N_2$  will get a small NLM weighting, therefore minimizing its influence on the outcome of the estimation. On the other hand,  $N_1$  and  $N_3$  are very similar, and therefore should be retained in the estimation. Furthermore, the pattern of  $N_4$ , under linear regression, is also similar to that of  $N_1$  and  $N_3$ , and would contribute to the final estimation of the intensity pattern as well. As mentioned in the previous section, we retain the simple edge detection scheme from the original NEDI method to alleviate the computation load. Moreover, the computation is carried

```

Initializing: setting threshold values; setting k=1
For each pixel  $y$  to be interpolated, do
{
  If ( $k=1$ )
     $\alpha^{(0)} = \arg \min_{\alpha^{(0)}} \sum_i (r_i^{(0)})^2$ 
  else ( $k>1$ )
     $\omega^R(r_i^{(k-1)}) = \exp(-\frac{(r_i^{(k-1)})^2}{c^2})$ ,  $\omega_i^N = \exp(-\frac{\|N^i - N^{current}\|^2}{h^2})$ 
     $\alpha^{(k)} = \arg \min_{\alpha^{(k)}} \sum_i \omega_i^N \cdot \omega^R(r_i^{(k-1)}) \cdot (r_i^{(k)})^2$ 
}
 $y = \alpha \cdot [y_1 \quad y_2 \quad \cdots \quad y_n]^T$ 

```

**Figure 6.** The pseudo-code for the NLM weighted IRLS fitting.

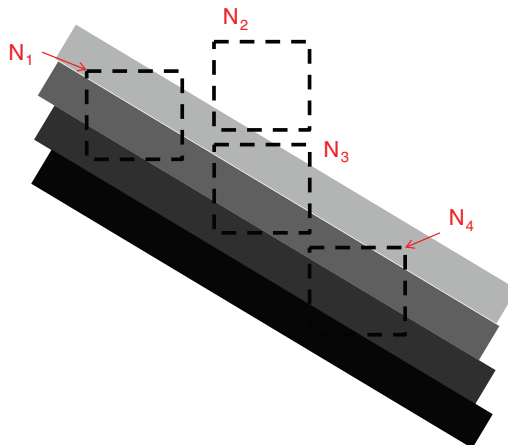


**Figure 7.** A simple example to demonstrate the ability of our method to distinguish between neighborhoods of different patterns.

out in a neighborhood of 7 by 7 pixels, which we have found to be a good balance between computation load and algorithm performance.

### 3. Results and discussion

#### 3.1. Experimental setup

In this section, we present the results for our robust NEDI (R-NEDI), as compared to bicubic interpolation and NEDI, on geometric phantom images, synthetic images (from Brainweb

(Collins *et al* 1998)) and real MR images. The original 2D images, including the slices from the 3D volumes for both synthetic and real images, were of a dimension of  $256 \times 256$ , downsampled by a factor of 4, adding Rician noise of varying levels, and then used as the input for different interpolation methods. For real diffusion MR images, we show here the results from a real rat brain atlas of size  $256 \times 256 \times 21$ , with six gradient directions, each with seven repetitions,  $b_0 = 800 \text{ s mm}^{-2}$ . It is important, however, to note that no special treatment is taken regarding the correlation between channels of the multi-valued DW images, i.e. each channel is interpolated independently. While the inter-channel correlation can be exploited to produce better interpolation results for certain multi-valued images (e.g. color images in Tschumperle and Deriche (2002) and diffusion tensor (DT) images in Zhenhua *et al* (2010)), we here emphasize more on the impact of a certain methodology on the scalar-valued images.

For numerical evaluation, we use PSNR and structural similarity index (SSIM) (Wang *et al* 2004) for comparing the scalar image interpolation. For each measurement of PSNR or SSIM of the interpolated images, five interpolations with different noise were carried out to obtain the mean value. For evaluation of DT images that resulted from the interpolation for the DWI, we used the overlapping of eigenvalue/eigenvector pairs (OVL) (Basser and Pajevic 2000b) to measure how well the interpolation is in agreement with the ground truth.

### 3.2. Geometric phantom image

Firstly, for the phantom images, the interpolation results for three different methods with Rician noise (standard deviation ranging from 5% to 40% of the image mean intensity) are shown in figure 8. As demonstrated in figure 8, both edge-directed methods are able to better capture the edges which the bicubic method renders as jagged ones. However, due to the limitations of NEDI discussed in section 2.2, the NEDI result features artifacts around the thin edges, which become worse as the noise level increases. The explanation for this behavior of NEDI is rooted in its OLS scheme: it treats all neighbors inside a local region with equal importance, regardless of whether they belong to the same edge pattern or not. Consequently, the edge pattern estimated by NEDI will not truly reflect the real one. This drawback becomes apparent when the neighborhood contains small and/or thin edge patterns, and it is further exacerbated by the presence of the noise, as shown in figure 8. In comparison, R-NEDI not only corrects for that, but also better preserves the shape of the rings, even for high noise levels.

### 3.3. Synthetic and real images

For synthetic images, the results (with Rician noise from 5% to 20%) are shown in figure 9. Again the bicubic results feature jagged edges and distorted image structures (as with heavy noise). The NEDI method is able to eliminate the jagged artifacts, yet as the noise increases, it produces unnatural texture-like artifacts. By contrast, our improved algorithm not only retains the edge-preserving ability, but it can also reproduce the image structures more consistently, even in the case of heavy noise. The PSNR and SSIM comparison for synthetic images in figure 11 demonstrates quantitative evidence to the qualitative observation above.

As for real scalar images, combining figure 10 and figure 11, a steady trend is the deterioration of the interpolations with increasing noise level, which is to be expected. Interestingly, the bicubic method does not necessarily produce worse results than NEDI. For example, when the noise level is 10%, the PSNR and SSIM for the bicubic method are

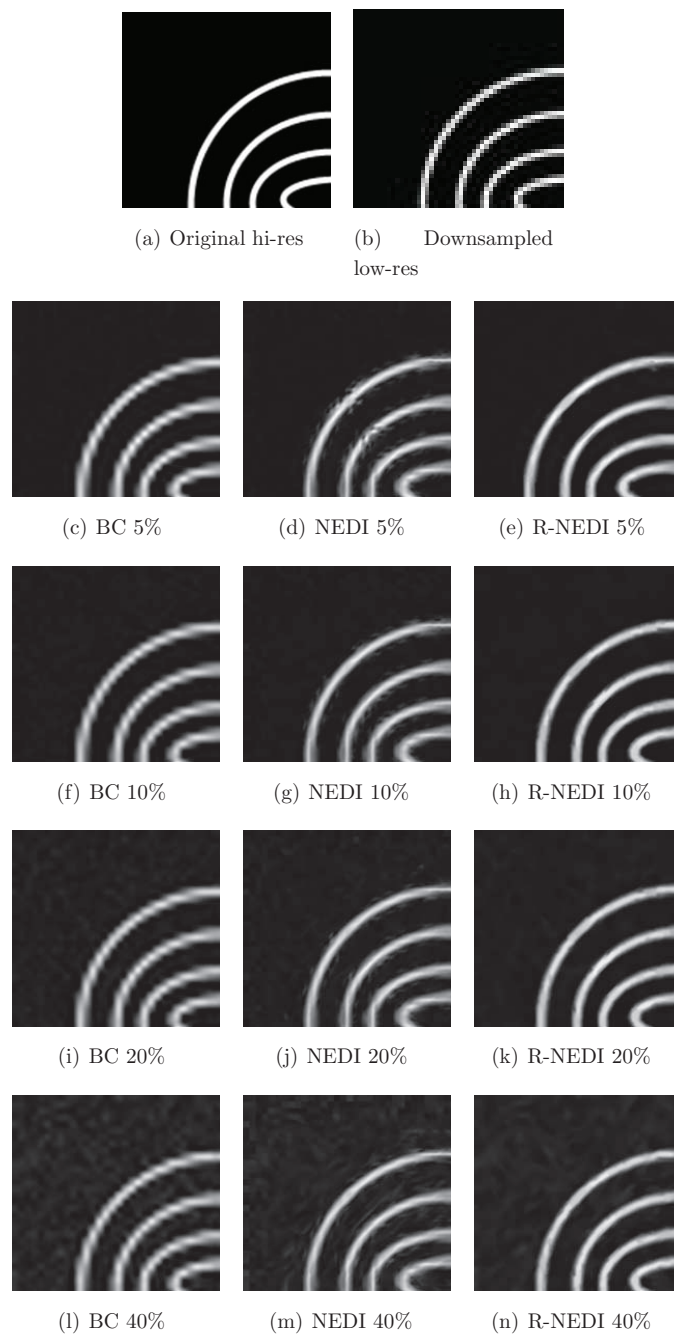


**Figure 8.** The comparison of interpolations on a phantom image of dense thin edge patterns. Top row: from left to right are the original, HR image and the downsampled, LR image. Bottom rows: from left to right are the bicubic interpolation, NEDI result and R-NEDI result, respectively. From second top row to bottom, Rician noise is added in the downsampled images in each row. The standard deviations of the noise are set to be 5%, 10%, 20% and 40% of the mean image intensity, respectively.

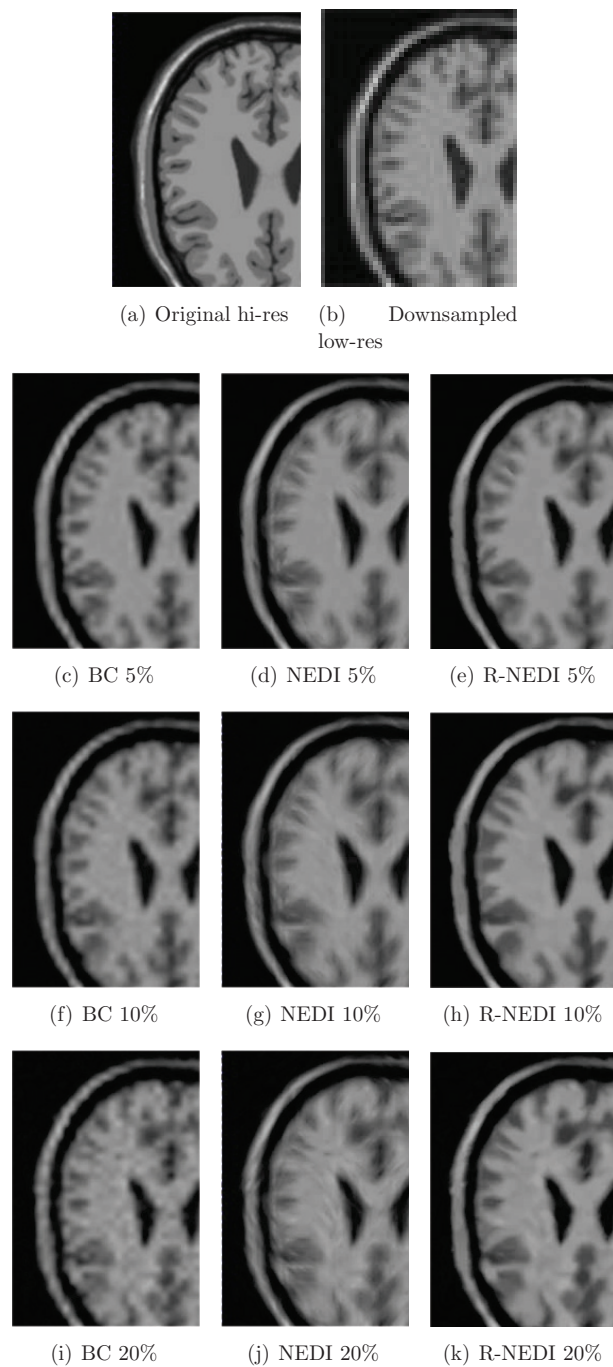


**Figure 9.** The comparison of interpolations on a synthetic brain image from Brainweb. Top row: from left to right are the original, HR image and the downsampled, LR image. Bottom rows: from left to right are the bicubic interpolation, NEDI result and R-NEDI result, respectively. From second top row to bottom, Rician noise is added in the downsampled images in each row. The standard deviations of the noise are set to be 5%, 10% and 20% of the mean image intensity, respectively.

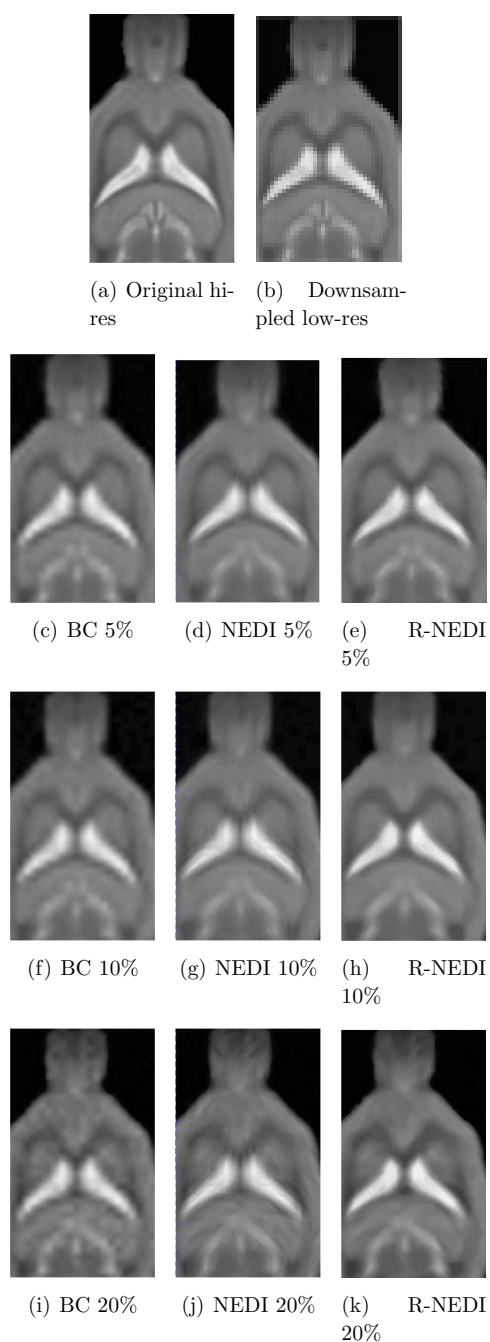


**Figure 10.** The comparison of interpolations on a real rat brain image. Top row: from left to right are the original, HR image and the downsampled, LR image. Bottom rows: from left to right are the bicubic interpolation, NEDI result and R-NEDI result, respectively. From second top row to bottom, Rician noise is added in the downsampled images in each row. The standard deviations of the noise are set to be 5%, 10% and 20% of the mean image intensity, respectively.

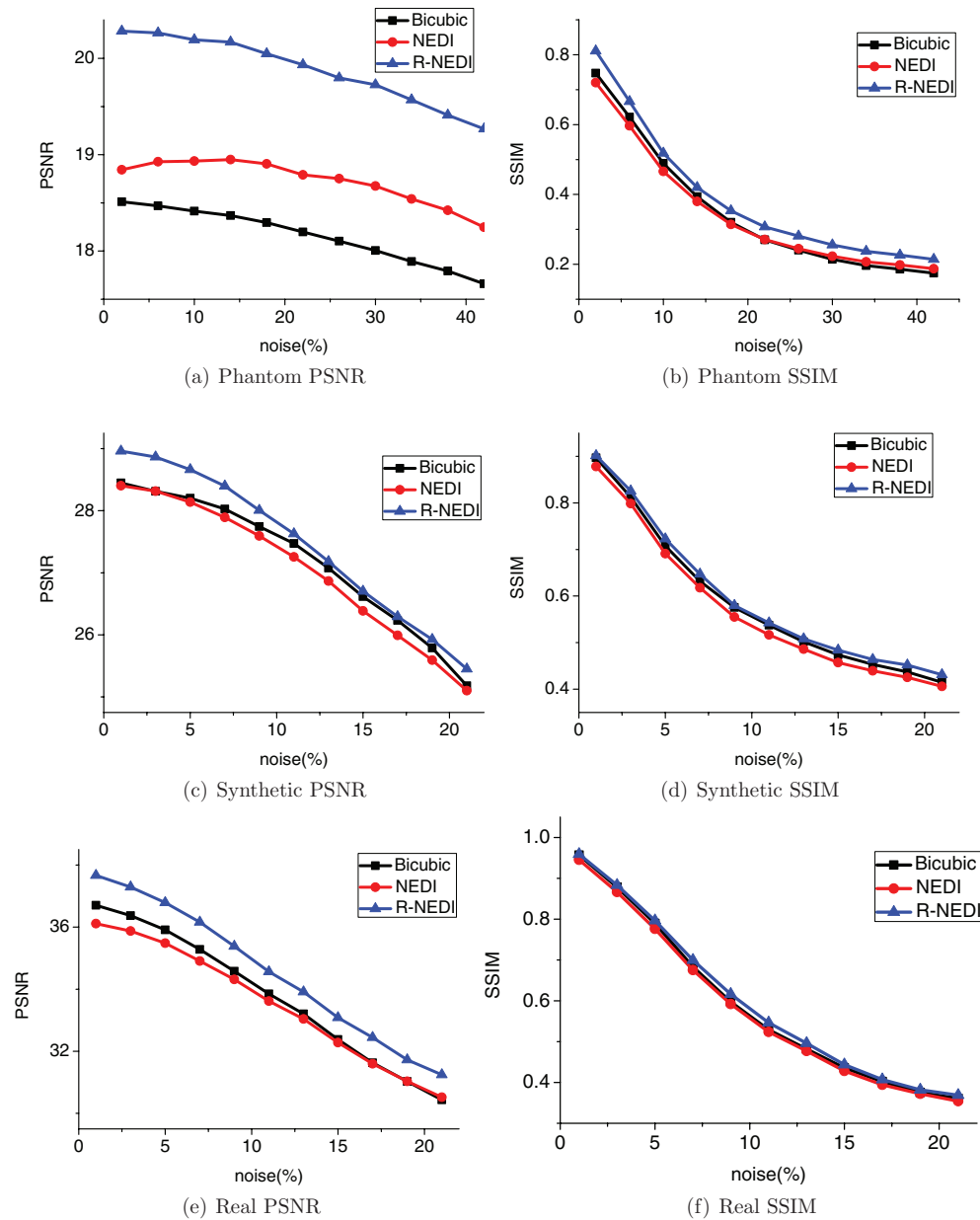


**Figure 11.** PSNR and SSIM comparison of interpolations for phantom, synthetic and real images. For phantom images, Rician noise from 2% to 40% is added, while for synthetic and real images, Rician noise from 2% to 20% is added. On the left column, (a), (c) and (e) are the PSNR comparisons for phantom image, synthetic image and real image, respectively. On the right column, (b), (d) and (f) are the corresponding SSIM comparisons. Black lines are for the bicubic results, red lines the NEDI results, and blue lines the R-NEDI results. Measurements are carried out five times, with mean values shown here. Error bars are omitted because the standard deviations of measurements are insignificant compared to the mean values.

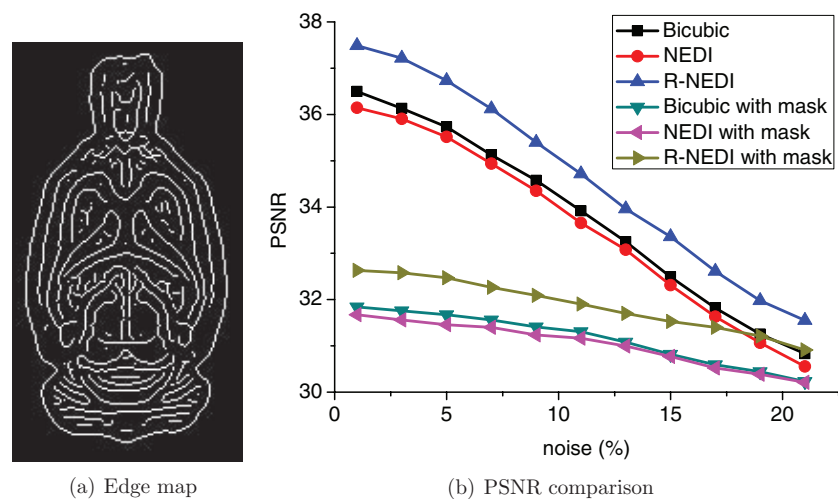


**Figure 12.** Algorithm evaluation with edge masking. (a) The edge map generated with the Canny edge detector on a real image. (b) The PSNR comparison between bicubic, NEDI and R-NEDI with and without the edge masking. Rician noise from 2% to 20% is added.

34.6 and 0.597, respectively, both better than those of NEDI, 34.3 and 0.592, respectively. Visually, it is not difficult to find fault in the bicubic interpolations, as evidenced by the jagged edges around the structure boundaries. However, despite the absence of jagged edges, NEDI produces blurred edges, as well as the textures similar to the synthetic case. In comparison, R-NEDI (35.4 and 0.616 for PSNR and SSIM) produces smooth and defined edges, while texture artifacts caused by the noise are still largely under control.

The efficiency of the algorithm can also be demonstrated by its performance exclusively on the ‘edge’ pixels. The edge pixels are detected with one of the widely used methods, Canny detector (Canny 1986), on the real image, as shown in figure 12(a). Figure 12(b) shows that the PSNR of the three methods we compared with and without edge masking, with respect to varying levels of Rician noise. It is shown that the interpolation error increases in general with an edge masking (overall drop in the PSNR), which is quite understandable given the fast changing statistics around edge points and henceforth the associated difficulty of capturing them. However, our edge-directed method is still able to reproduce the edge structure more accurately than either the bicubic interpolation or NEDI.

Finally, we show the FA overlay, as well as the OVL, in figure 13. The FA map of the DTI estimated from the interpolated DWI is given a color code of green. The ground truth FA map (estimated from the ground truth DTI which is derived from the ground truth DWI) is given red. Both are overlaid onto each other, resulting in the FA overlay map. Wherever the interpolation results do not agree with the ground truth, the overlay map will show a patch of either red or green. The comparison shows that the R-NEDI result shows fewer red/green patches, whose presence indicates the inaccuracy of interpolation. As mentioned before, DW images (and henceforth DT images) contain a lot of orientational information that is encoded in the image structures. Non edge-preserving methods will have difficulty in preserving and reproducing the structural information, and further lose the valid orientational information inherent in the DW images, as evidenced in the FA overlay figure. This further demonstrates visually that the robust edge-preserving ability of our R-NEDI method can translate into the preservation of the essential structural information of the DW images.

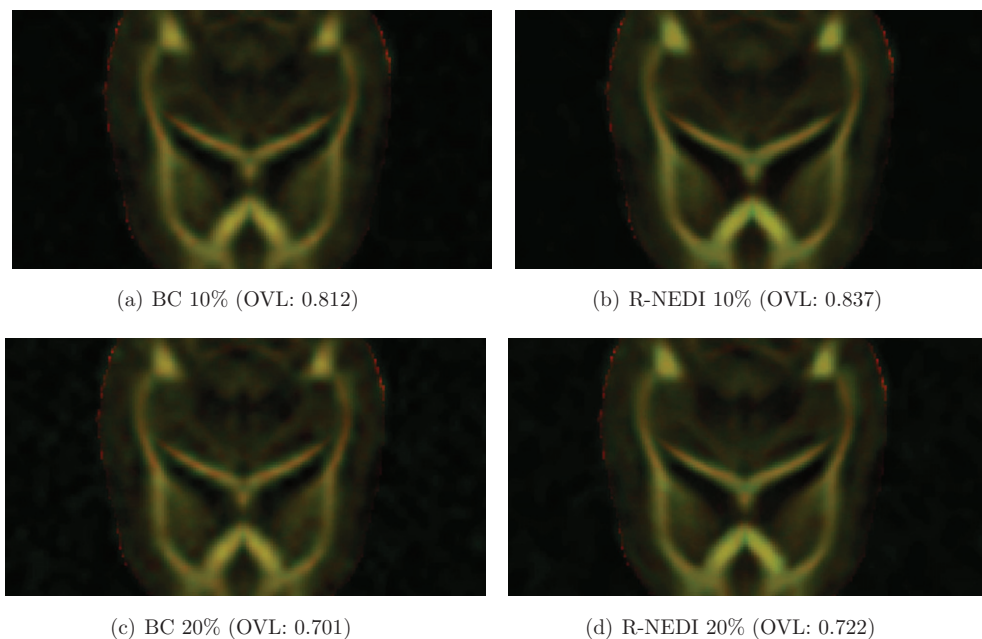


**Figure 13.** Comparison of the FA overlay with the DT images as estimated from the interpolated DWI. The FA maps for interpolations are estimated from the DT images that are estimated from the corresponding DWI interpolations. The ground truth FA map is estimated similarly from the ground truth DWI. From left to right are the bicubic interpolation and R-NEDI result, respectively. From top to bottom, the standard deviations of the added Rician noise are set to be 10% and 20% of the mean image intensity, respectively. OVL as a measure of the similarity between the interpolation and the ground truth is included in the brackets.

#### 4. Conclusion

In this work, we have improved upon NEDI based on our new understanding for its least-squares fitting nature, and extended the edge-directed concept onto the diffusion MR image interpolation. The source of non-robustness of NEDI was identified and improvements were suggested accordingly. Our improvements on the original NEDI not only strengthen its ability to implicitly retain the edge information, but also make it more robust to noise. Our experiments have demonstrated that R-NEDI produces superior results compared to conventional interpolation methods. Moreover, its robust ability to reconstruct the fine details about image structures also makes it suitable for use in certain feature-dense image processing tasks, e.g. atlas construction (Van Hecke *et al* 2008), where registration could benefit from a more accurate and robust interpolation of the images. As for prospective works, this edge-directed concept for diffusion MR image interpolation can be further investigated with more robust models for least-squares estimation. Furthermore, it could also be extended to interpolate on arbitrary spatial points.

#### Acknowledgments

This work was financially supported by the Inter-University Attraction Poles Program 6-38 of the Belgian Science Policy, and by the SBO-project QUANTIVIAM (060819) of

the Institute for the Promotion of Innovation through Science and Technology in Flanders (IWT Vlaanderen). The authors would also like to thank Wolfgang Jacquet for his useful discussions.

## References

- Allebach J and Wong P 1996 Edge-directed interpolation *Proc. IEEE Int. Conf. Image Process.* **3** 707–10
- Basser P and Pajevic S 2000a Statistical artifacts in diffusion tensor MRI (DTMRI) caused by background noise *Magn. Reson. Med.* **44** 41–50
- Basser P J and Pajevic S 2000b Statistical artifacts in diffusion tensor MRI (DT-MRI) caused by background noise *Magn. Reson. Med.* **44** 41–50
- Buades A, Coll B and Morel J M 2005 A non-local algorithm for image denoising *IEEE Comput. Vis. Pattern Recognit.* **2** 60–5
- Canny J 1986 A computational approach to edge detection *IEEE Trans. Pattern Anal. Mach. Intell.* **8** 679–98
- Chao T, Chou M, Yang P, Chung H and Wu M 2009 Effects of interpolation methods in spatial normalization of diffusion tensor imaging data on group comparison of fractional anisotropy *Magn. Reson. Imaging* **27** 681–90
- Collins D L, Zijdenbos A P, Kollokian V, Sled J G, Kabani N J, Holmes C J and Evans A C 1998 Design and construction of a realistic digital brain phantom *IEEE Trans. Med. Imaging* **17** 463–8
- Gudbjartsson H and Patz S 1995 The Rician distribution of noisy MRI data *Magn. Reson. Med.* **34** 1522–2594
- Holland P W and Welsch R E 1977 Robust regression using iteratively reweighted least-squares *Commun. Stat.: Theory Methods A* **6** 813–7
- Jayant N and Noll P 1984 *Digital Coding of Waveforms: Principles and Application* (Upper Saddle River, NJ: Prentice-Hall)
- Jensen K and Anastassiou D 1995 Subpixel edge localization and the interpolation of still images *IEEE Trans. Image Process.* **4** 285–95
- Keys R 1981 Cubic convolution interpolation for digital image processing *IEEE Trans. Acoust. Speech Signal Process.* **29** 1153–60
- Lee S and Paik J 1993 Image interpolation using adaptive fast B-spline filtering *Proc. IEEE Int. Conf. Acoust. Speech Signal Process.* **5** 177–80
- Lehmann T, Gonner C and Spitzer K 1999 Survey: interpolation methods in medical image processing *IEEE Trans. Med. Imaging* **18** 1049–75
- Li X and Orchard M T 2001a Edge directed prediction for lossless compression *IEEE Trans. Image Process.* **10** 813–27
- Li X and Orchard M T 2001b New edge directed interpolation *IEEE Trans. Image Process.* **10** 1521–7
- Mai Z, Verhoye M, Van der Linden A and Sijbers J 2010 Diffusion tensor image upsampling: a registration-based approach *Magn. Reson. Imaging* **28** 1497–506
- Manjón J V, Caballero J C, Lull J J, Martí G G, Bonmatí L M and Robles M 2008 MRI denoising using non-local means *Med. Image Anal.* **12** 514–23
- Meijering E 2002 A chronology of interpolation: from ancient astronomy to modern signal and image processing *Proc. IEEE* **90** 319–42
- Morse B S and Schwartzwald D 1998 Isophote-based interpolation *Proc. IEEE Int. Conf. Image Process.* **3** 227–31
- Thévenaz P, Blu T and Unser M 2000 Image interpolation and resampling *Handbook of Medical Image* ed N Bankman (Orlando, FL: Academic) pp 393–420
- Tschumperle D and Deriche R 2002 Diffusion PDE's on vector-valued images: local approach and geometric viewpoint *IEEE Signal Process. Mag.* **19** 16–25
- Van Hecke W, Sijbers J, D'Agostino E, Maes F, De Backer S, Vandervliet E, Parizel P M and Leemans A 2008 On the construction of an inter-subject diffusion tensor magnetic resonance atlas of the healthy human brain *Neuroimage* **43** 69–80
- Wang Q and Kreidieh R 2007 A new orientation-adaptive interpolation method *IEEE Trans. Image Process.* **16** 889–900
- Wang Z, Bovik A C, Sheikh H R and Simoncelli E P 2004 Image quality assessment: from error visibility to structural similarity *IEEE Trans. Image Process.* **13** 600–12
- Zhang Z 1997 Parameter estimation techniques: a tutorial with application to conic fitting *Image Vis. Comput.* **15** 59–76
- Zhenhua M, Jacquet W, Verhoye M and Sijbers J 2010 Diffusion tensor images edge-directed interpolation 2010 *IEEE Int. Symp. on Biomedical Imaging: From Nano to Macro* pp 732–5